PCCP

ROYAL SOCIETY OF CHEMISTRY

PAPER

View Article Online
View Journal | View Issue

Cite this: *Phys. Chem. Chem. Phys.*, 2023, **25**, 16363

The photogalvanic effect induced by quantum spin Hall edge states from first-principles calculations

Yaqing Yang,[ae] Liwen Zhang,[b] Xiaohong Zheng,*[c] Jun Chen,[de] Liantuan Xiao,[ae] Suotang Jia[ae] and Lei Zhang *[ae]

Received 13th February 2023,
Accepted 18th May 2023

DOI: 10.1039/d3cp00695f

rsc.li/pccp

Based on non-equilibrium Green's function combined with density functional theory (NEGF-DFT), we theoretically investigate the spin-related photogalvanic effect (PGE) in topological insulators BiBr and SbBr nanoribbons from atomic first-principles calculations. It is demonstrated that the PGE generated photocurrents by quantum spin Hall edge states (QSHES) are in general pure spin currents due to the presence of time reversal and mirror symmetries, which is independent of the photon energies, polarization, and incident angles. Although the QSHES are topologically protected and robust against defects and impurities during their transport, the spin photocurrent generated by these edge states *via* the PGE is particularly sensitive to defects. By tuning the defect position of the nanoribbons, the magnitude of spin related photocurrent generated by the PGE can be significantly increased compared with that in pristine nanoribbons. Our work not only reveals the defect effect of PGE but also demonstrates the great potential of defect engineered topological insulator nanoribbons for novel application in two-dimensional opto-spintronic devices.

1 Introduction

Topological insulators (TIs) have attracted growing research attention in the fields of condensed matter physics and materials science.[1–7] Inside, the topological insulators are non-conductive like ordinary insulators but there are always conductive edge states on their boundary or surface in two or three-dimensional systems.[4,8–12] The edge state of a topological insulator is entirely determined by the topological properties of the corresponding bulk electronic state of the material, which is usually determined by symmetry, and does not depend on the specific atomic structure of the surface. Therefore, the edge states on the surface of a topological insulator are topologically protected and are basically not affected by impurities and defects during their transport.[4,9,10,13–16] In addition, at the edge of topological insulators, electrons with different spins move in opposite directions, so the spin degrees of freedom of the electrons can be used as transport information carriers.[4,17] Compared with the traditional transfer of information through electric charge, this process ideally has no energy loss, which provides a new direction for the design of spintronic devices with low energy dissipation. The discovery and application of topological insulators have brought tremendous changes to electronics and microelectronics, and they have potential applications in the design of new two-dimensional electronic devices.[18–24] In recent years, due to the development of topological physics theory and the excellent photoelectric properties of two-dimensional materials, two-dimensional topological materials represented by quantum spin Hall (QSH) insulators have attracted much attention.[25–28] At present, the quantum spin Hall effect has been experimentally realized in HgTe/CdTe and InAs/GaSb/AlSb quantum wells.[29–32] However, since they have very small bulk bandgaps, it requires extremely low temperatures to observe the expected QSH effect. Therefore, finding a two-dimensional topological insulator with a large bandgap is an important research direction.

More recently, based on phonon mode and finite temperature molecular dynamics and first-principles calculations, BiBr and SbBr have been proven to be stable TIs with a large bandgap, and the edge defects have no effect on the transport of the edge states.[33,34] Lately, there have been reports about the photogalvanic effect (PGE) in TIs;[35–39] nevertheless, whether

[a] *State Key Laboratory of Quantum Optics and Quantum Optics Devices, Institute of Laser Spectroscopy, Shanxi University, Taiyuan 030006, China. E-mail: zhanglei@sxu.edu.cn*
[b] *School of Physics and Information Engineering, Shanxi Normal University, Taiyuan 030031, China*
[c] *College of Information Science and Technology, Nanjing Forestry University, Nanjing 210037, China. E-mail: xhzheng@theory.issp.ac.cn*
[d] *State Key Laboratory of Quantum Optics and Quantum Optics Devices, Institute of Theoretical Physics, Shanxi University, Taiyuan 030006, China*
[e] *Collaborative Innovation Center of Extreme Optics, Shanxi University, Taiyuan 030006, China*

the photocurrent generated by the PGE is robust has not been explored. Since the inversion symmetry of bulk BiBr and SbBr is preserved, it will be interesting to know if the pure spin photocurrent can be generated *via* PGE in TIs BiBr and SbBr nanoribbons. If possible, is the spin photocurrent robust against defects or not? Does the spin photocurrent produced by PGE depend on the vacancy defect's location? Can the PGE induced spin dependent photocurrent be further tuned?

In this work, we demonstrate the effect of vacancy defects on the spin dependent photocurrent produced by linearly polarized light PGE in TIs BiBr and SbBr nanoribbons by using first-principles calculations. It is found that, the pure spin photocurrent can be generated *via* the photogalvanic effect, which is independent of the photon energies, polarization, and incident angles. However, the spin photocurrent is not robust against vacancy defects, which can increase the spin dependent photocurrent generated *via* PGE by about 100 times. In addition, the spin dependent photocurrent can be largely tuned by varying the defect position of the nanoribbons. Therefore, our work demonstrates the great potential of topological nanoribbons for novel application in two-dimensional opto-spintronic devices.

2 Theoretical formalism and computational details

The atomic structures of the two-probe device based on the TIs BiBr and SbBr nanoribbons are presented in Fig. 1, where the system has mirror symmetry along the x-direction and no inversion symmetry due to the presence of edges. The device can be divided into three regions in the numerical simulation: the central scattering region and the left and right leads extending to the electron reservoirs in the infinity to collect current. For a nanoribbon with width $W = 8$, there are 5.5 unit cells with a total of 176 atoms in the central scattering region to ensure the symmetry of the system. The vacuum layers of sufficient length are set to avoid the fake interaction between neighboring slabs along the y-direction and the z-direction. In numerical calculations, the x axis is the electron transport direction, while the y axis is along the width of the nanoribbon and the z axis is perpendicular to the two-dimensional system.

Before analyzing the quantum transport properties of the TIs BiBr and SbBr nanoribbons, the atomic structures are fully relaxed until the forces acting on each atom are less than 0.01 eV Å^{-1} by using Vienna ab initio simulation package (VASP).[40] The first Brillouin zone of the unit cell for the nanoribbon is sampled by a 11 × 1 × 1 k space grid during the calculations, and the energy cutoff of 500 eV is used for the plane-wave expansion. The calculations of quantum transport are performed by using the Keldysh non-equilibrium Green's function (NEGF) formalism[41–44] combined with DFT, as implemented in the first principles quantum transport package Nanodcal.[41,45–47] In the NEGF-DFT self-consistent calculations, the linear combination of atomic orbital (LCAO) basis at the double-ζ polarization (DZP) level is used to expand the wave functions and the other physical quantities; the atomic core are

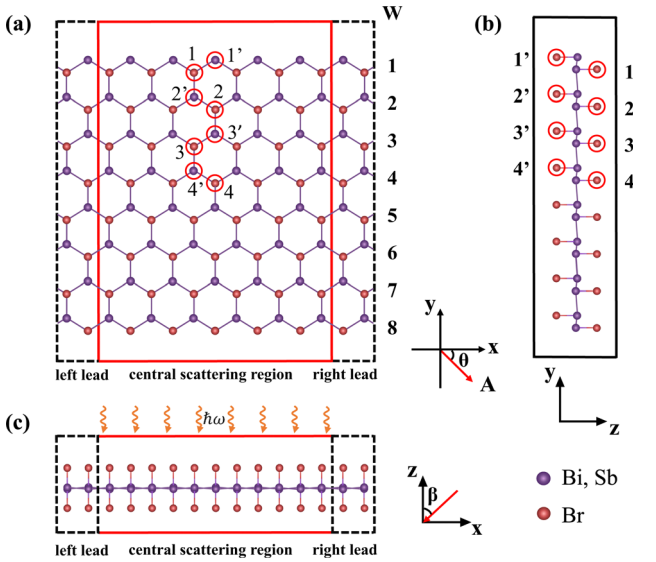

Fig. 1 (a–c) Schematic plot of a two-probe device atomic structure constructed using BiBr/SbBr nanoribbons with width W= 8. (a) Top view (b and c) side view for the y–z and x–z plane, respectively. There are three parts in the system, the left and right leads and the central scattering region where the light with photon energy $E_{ph} = \hbar\omega$ is shining. The purple and red spheres represent Bi/Sb and Br atoms, respectively. The red circle indicates the position of the vacancy defect where the Br atom is removed. Here A is the electromagnetic vector potential inside the x–y plane, θ denotes the polarization angle for the linearly polarized light with respective to the x direction and β is the corresponding photon incident angle with respective to the z direction.

described by the standard norm-conserving nonlocal pseudopotentials;[48] the generalized gradient approximation (GGA) with the Perdew–Burke–Ernzerhof (PBE) functional is applied for the exchange-correlation potential.[49] The NEGF-DFT self-consistency is deemed achieved when the monitored quantities such as every element of the Hamiltonian and density matrices differs by less than 1×10^{-6} a.u. between iteration steps.

For the two-probe device (see Fig. 1), the spin dependent photocurrent could be generated by the linearly polarized light shining on the central scattering region which is indicated by the box drawn with a red solid line. Moreover, the direction of the current flows from the electrode to the central region. In the following, we consider the photocurrent flowing in the left electrode of the two-probe structure. The electron–photon interaction is treated as a perturbation during our study. Our assumption is based on weak electromagnetic interaction, which does not appreciably disturb the single-particle state. Thus, the self-consistent calculation of electron density is performed without considering the electron–photon interaction. Moreover, only single photons even enter the physical process since the multi-photon process would be a very low-probability process when the photon field is weak.[50] After obtaining the NEGF-DFT self-consistent device Hamiltonian, the spin dependent photocurrent $J_{L,s}^{(ph)}$ can be expressed as the following formula,[46,51]

$$J_{L,s}^{(ph)} = \frac{ie}{h}\int \mathrm{Tr}\left\{\Gamma_L\left[G_{ph}^{<} + f_L(\varepsilon)\left(G_{ph}^{>} - G_{ph}^{<}\right)\right]\right\}_{ss} \mathrm{d}\varepsilon, \qquad (1)$$

where L indicates the left electrode and s indicates the spin component (s= ↑,↓); $\Gamma_L = i(\Sigma_L^r - \Sigma_L^a)$ and $f_L(\varepsilon)$ are the linewidth function and the Fermi–Dirac distribution function of the left lead; $\Sigma_L^r = [\Sigma_L^a]^\dagger$ is the retarded self-energy due to the presence of the left lead; $G_{ph}^{</>} = G_0^r \Sigma_{ph}^{</>} G_0^a$ is the lesser/greater Green's function including electron–photon interaction,[50,52–55] where $\Sigma_{ph}^{</>}$ is the self-energy due to the presence of the electron–photon interaction. The information about the polarization of light is included in the self energy and can be characterized by a complex vector e. For the linearly polarized light, $e = \cos\theta e_1 + \sin\theta e_2$, where θ is the angle formed by the polarized direction with respect to the vector e_1 as shown in Fig. 1. In our numerical calculations, the vectors e_1 and e_2 are set along the x and $-y$ directions and the light is incident along the $-z$ direction with different incidence angles β as shown in Fig. 1.

For simplicity, we introduce a normalized photocurrent[50,51] with respective to the photon flux, *i.e.*,

$$R_s = \frac{J_{L,s}^{(ph)}}{eI_\omega}, \tag{2}$$

where $J_{L,s}^{(ph)}$ is the spin dependent photocurrent defined in eqn (1); I_ω is the photon flux defined as the number of photons per unit time per unit area. Note that the photoresponse has dimension of area, a_0^2/photon where a_0 is the Bohr radius. In order to characterize the imbalance of the generated spin dependent photoresponse, the spin polarization (SP) is defined as,

$$\mathrm{SP}(\%) = \frac{|R_\uparrow - R_\downarrow|}{|R_\uparrow + R_\downarrow|} \times 100, \tag{3}$$

where $R_{\uparrow/\downarrow}$ represents the photoresponse of the left lead for spin up/down component, respectively.

3 Results and discussion

To start with, we investigate the electronic structure and dc transport properties of BiBr and SbBr nanoribbons with width W = 8 as an example. The corresponding band structures are shown in Fig. 2(a and e). The QSHES are located inside the energy range [−0.25,0.48] eV and [−0.35,0.67] eV for BiBr and SbBr nanoribbons, which are doubly degenerated due to the presence of time reversal symmetry. When the electron energy is less than −0.25 eV, the states of the valence band extend to the center of the nanoribbon, which can be found in LDOS as shown in Fig. 2(g). To illustrate the robustness of these QSHES, we calculated the transmission spectrum of the nanoribbons with or without vacancy defects in the nanoribbon. Here, the vacancy defect is represented by removing a Br atom in different locations presented in Fig. 1(a and b). It can be clearly seen that the vacancy defect at different positions does not lead to any observable effect on the transmission with QSHES of BiBr nanoribbons, which are still quantized and robust against defects. In contrast, the transmission with bulk states changes

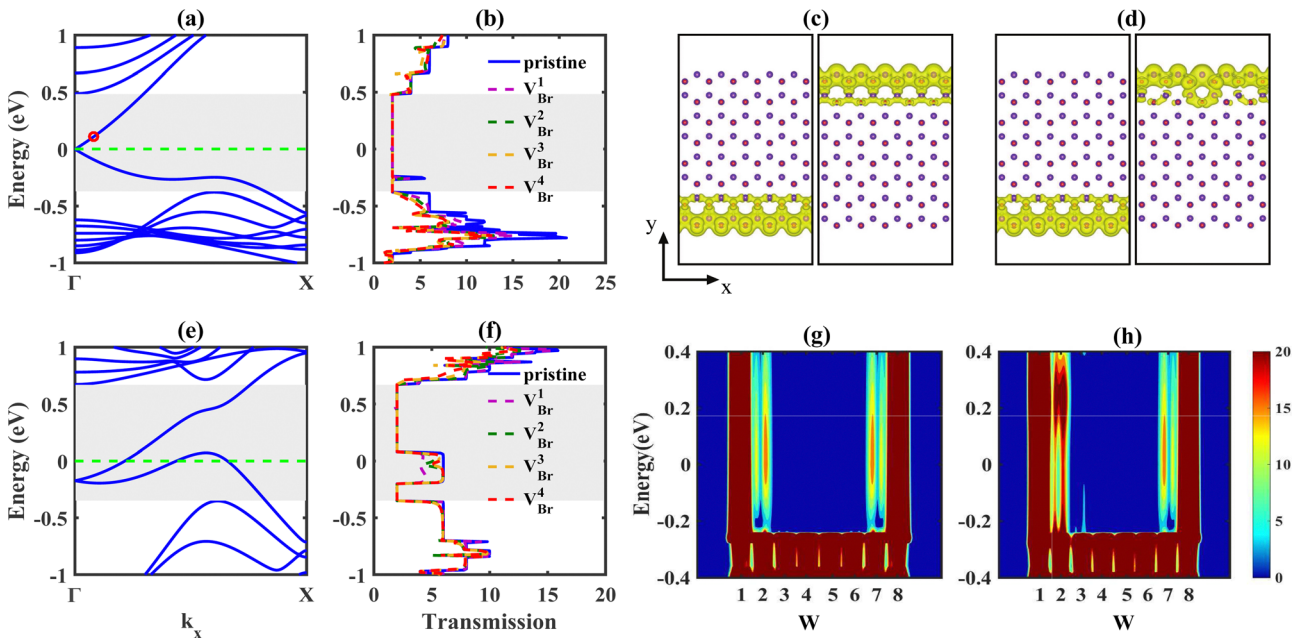

Fig. 2 (a and e) The band structure of a BiBr/SbBr nanoribbon with width W = 8. The horizontal dashed green line represents the Fermi energy. (b and f) The corresponding transmission coefficient with/without defect *versus* the electron energy. Here the blue line corresponds to the transmission coefficient of the pristine ribbon. The dotted lines with different colors represent the transmission coefficient when a vacancy defect is introduced at the position shown in Fig. 1 (a). The shadow region denotes the bandgap. (c and d) The isosurface plot of scattering states with two injecting channels from the left lead of BiBr nanoribbon in the central scattering region without defect and with defect 1′, respectively. Here the energy E = 0.1 eV denoted as red circles in panel (a). (g and h) The local density of states (LDOS) of the BiBr nanoribbon in the central scattering region *versus* the electron energy and transverse direction without defect and with defect 1′, respectively.

drastically with the presence of defects outside the bulk band-gap region. Comparatively, the transmission of SbBr nanoribbons between −0.19 eV and 0.07 eV is sensitive to the vacancy defect due to the formation of magnetic edge impurity, which introduces the backscattering in the system.[34] It is worth mentioning that the transmission is close to six when the vacancy approaches the center of nanoribbons, as shown in Fig. 2(f). As an illustration, we present the scattering states injected from the left lead in the central scattering region of the pristine BiBr nanoribbon at energy E = 0.1 eV in Fig. 2(c). Since they are QSHES, these states are doubly degenerated and distributed at the nanoribbon's upper and lower edges. As the vacancy defect is introduced in position 1′ in Fig. 2(d), the scattering state in the lower edge is unaffected. Although the distribution of the scattering state in the upper edge slightly changes, the corresponding transmission is still quantized without reflection. Next, we will study the effect of defects on the PGE-induced photocurrent with particular edge states involved to see if the photocurrent is still robust against defects.

After understanding the dc electronic properties of BiBr and SbBr nanoribbons, we first analyze the effect of defects on the spin dependent photoresponse of BiBr nanoribbons generated by linearly polarized light. It is known that the photocurrent can be generated in the system without inversion symmetry under light irradiation without the need for applying any external bias voltage. This phenomenon is dubbed as the photogalvanic effect (PGE) or the photovoltaic effect.[56–65] For nanoribbons, the inversion symmetry is inherently broken on the edges. However, the system preserves time-reversal symmetry and mirror symmetry along the x direction (M^x). According to the bulk spin photovoltaic effect,[66] it is expected that there is no charge photocurrent generated and the pure spin photocurrent can be produced in the transport direction of the studied topological insulator nanoribbons. As shown in Fig. 3(a and c), we find that the charge photoresponse R_c is indeed zero independent of photon energies in the topological insulator BiBr. However, the generated photoresponse for the spin up and spin down components are equal in magnitude and opposite in direction, which indicates that the pure spin photocurrent is produced. Furthermore, by tuning the polarization angle θ from 45° to 135°, the pure spin photocurrent can reverse its sign. Then we compare the photoresponse of the pristine nanoribbon and that with the defect location at 1′ by removing one Br atom at the boundary (see Fig. 1). When introducing the defect, we notice that the photoresponses of the spin-up and spin-down components increase significantly as shown in Fig. 3(b and d). At the same time, the obtained photocurrent is still close to the pure spin photocurrent, indicating that the large pure spin current can also be obtained using defect engineering. Unlike the robust dc transport properties against defects, the photoresponse for different spin components is quite sensitive to the presence of defects for both light polarization cases, indicating that the photoresponse is not topologically protected. In addition, we find that the magnitude of photoresponse generated by PGE in the defect

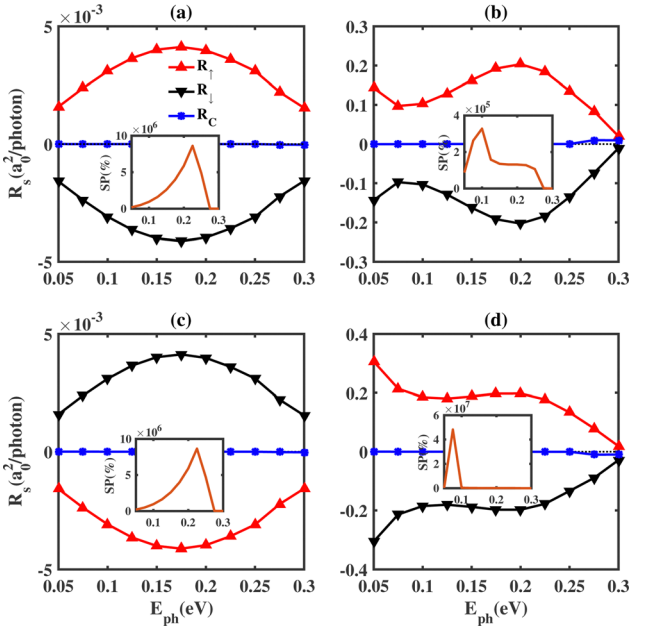

Fig. 3 The spin dependent photoresponse R_s *versus* the photon energy E_{ph} of the vertically incident linearly polarized light. (a and c) The calculated spin dependent photoresponse for a pristine nanoribbon when the photon polarization angle is fixed θ = 45° and θ = 135°, respectively. (b and d) The calculated spin dependent photoresponse for the nanoribbon with one Br atom (1′) removed when the photon polarization angle is fixed θ = 45° and θ = 135°, respectively. Insets in each panel are the corresponding spin polarization *versus* photon energies. Note that the light in all these cases is incident vertically. The width of the BiBr nanoribbon is fixed with W = 8. The red, black and blue lines represent the photoresponse for spin up, spin down and charge components.

case is usually much larger than that of the pristine system, the photoresponse can be 100 times larger. This is because the defect can further increase the asymmetry of the system and hence the photoresponse.[67]

Next, we study the influence of different defect positions on the photoresponse generated by LPGE where eight other places in the central scattering region as shown in Fig. 1. The numerical results are presented in Fig. 4. Although the photoresponse is sensitive to the defect positions, the photoresponses with defect positions from 2/2′ to 4/4′ have similar trends. For example, the photoresponses are relatively small when the incident photon energy is less than 0.25 eV. When the photon energy is greater than 0.25 eV, as the photon energy increases, the photoresponse gradually increases. When the defects are located in the first layer, the photoresponse is more significant than those in the other layers, as shown in Fig. 4(a and b). This is because the quantum spin Hall edge state is located at the boundary of the nanoribbon when the energy is less than 0.25 eV, as shown in Fig. 2(g). When the defect is located in the first layer, it will affect the distribution of the local density of states of the nanoribbon, so it has the greatest impact on the photocurrent. As the number of layers increases, the distribution of LDOS gradually approaches 0 as shown in Fig. 2(h), and the defect hardly affects the distribution of the local density of states, so it has little effect on the photocurrent. In order to further illustrate the impact of the

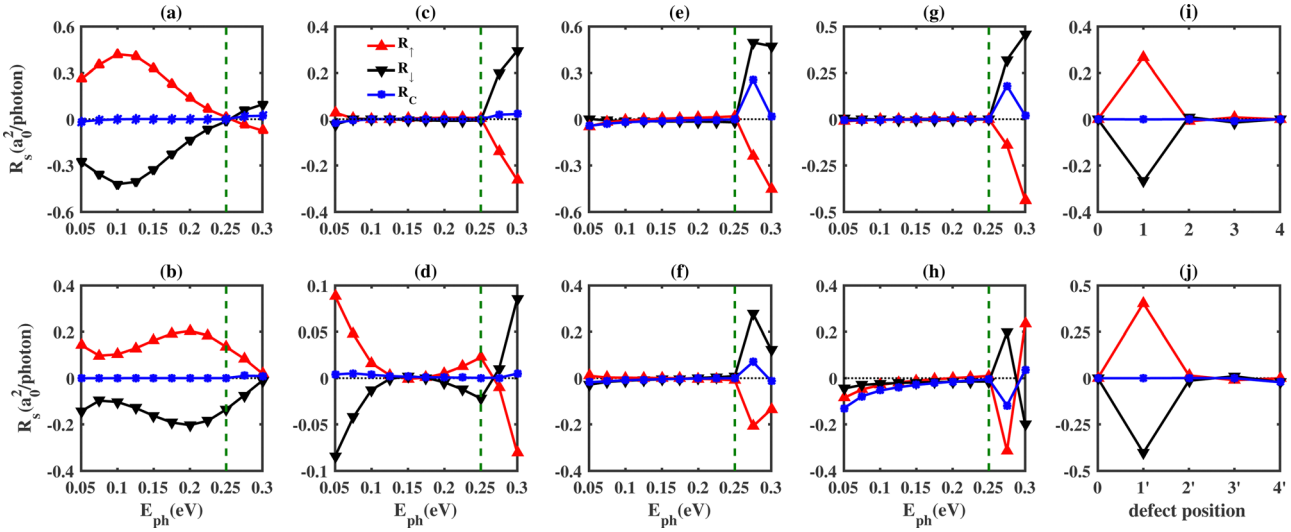

Fig. 4 The spin dependent photoresponse for the nanoribbon with one Br atom removed at different positions *versus* the photon energy E_{ph}. The positions of the defects are respectively located at (a) 1, (c) 2, (e) 3, (g) 4 and (b) 1′, (d) 2′, (f) 3′, (h) 4′ as shown in Fig. 1(a and b). (i and j) The spin dependent photoresponse *versus* the defect position when the incident photon energy is fixed at E_{ph} = 0.2 eV. The defect position at 0 means without defect. Here the linearly polarized light is vertically incident and the polarization angle θ is fixed $\theta = 45^\circ$ and the width of BiBr nanoribbon is W = 8. The red, black and blue lines represent the photoresponse for spin up, spin down and charge components.

defect position on the photoresponse, the photoresponse *versus* the defect position is studied and presented in Fig. 4(i) and (j) by fixing the incident photon energy as E_{ph} = 0.2 eV. It can be seen that the photoresponse is more prominent when the defects are located in the first layer. The photoresponse is smaller when the defects are located in the 2nd to 4th layer. Therefore, the photoresponse can be further tuned by the defect locations. In addition, when vacancy defects are introduced in the first layer, the photocurrent contributed by the edge states increases significantly due to the broken inversion symmetry of the system, but as the photocurrents for different spin components are almost equal in magnitude and opposite in direction, the spin polarization rate can reach 10^5%. Thus, the pure spin current can be obtained. This provides a novel approach to getting pure spin current in topological insulator nanoribbons.

Moreover, we study the effect of the polarization angle θ of LPGE and incident angle β on the spin dependent photoresponse for BiBr nanoribbons. Since the spin dependent photoresponse for $\theta = 45^\circ$ and $\theta = 135^\circ$ have distinct features, the photoresponse should sensitively depend on the light polarization θ. Thus, we investigate the spin dependent photoresponse *versus* the polarization angle θ. The numerical results are presented in Fig. 5(a) and (c). It can be seen that the spin dependent photoresponse can be greatly tuned by using the light polarization angle θ. When there are no defects, the pure spin current is obtained independent of the polarization angle. In general, the introduction of defects increases the spin-up and spin-down photoresponse components by two orders of magnitude. Therefore, the pure current generated by PGE can be significantly increased by introducing the defect in the system. Furthermore, we find that the spin dependent photoresponse can be further adjusted by the incident angle β as shown in Fig. 5(b) and (d). According to our investigations,

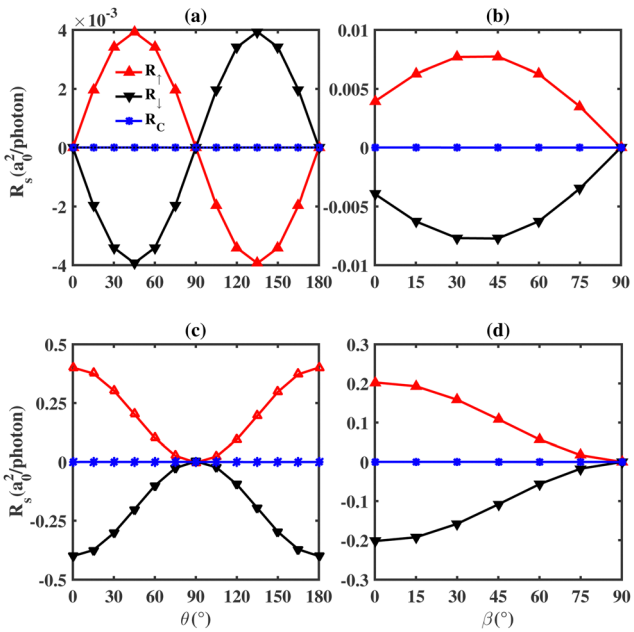

Fig. 5 (a and c) The spin dependent photoresponse *versus* the polarization angle θ of LPGE for the BiBr nanoribbon (a) without defect (c) with defect 1′. (b and d) The spin dependent photoresponse *versus* the photon incident angle β for BiBr nanoribbon (b) without defect (d) with defect 1′. Here, the width of the BiBr nanoribbon is W = 8, the incident photon energy is fixed at E_{ph} = 0.2 eV. The polarization angle was fixed at $\theta = 45^\circ$ in (b and d).

we find that the photoresponse *via* QSHES is also sensitive to the defect when the transport direction is along the armchair direction.

Last but not least, we discuss the PGE induced spin dependent photoresponse in SbBr nanoribbon to confirm the defect

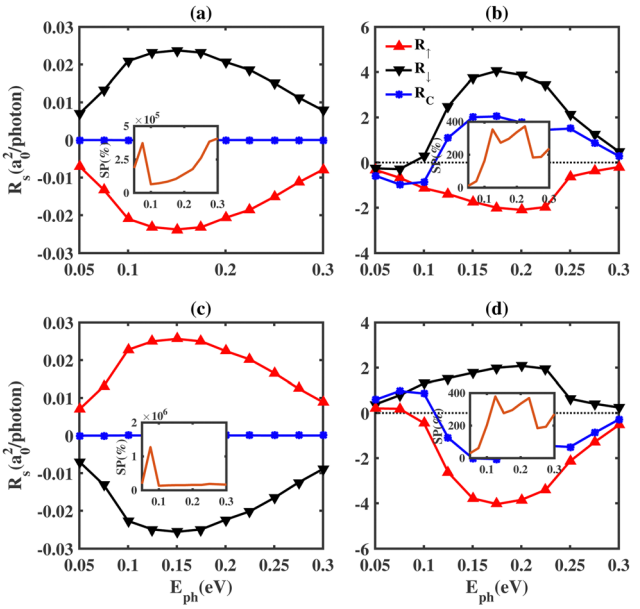

Fig. 6 The spin dependent photoresponse R_s *versus* the photon energy E_{ph} of the vertically incident linearly polarized light for SbBr nanoribbons. (a and c) The calculated spin dependent photoresponse for pristine nanoribbon when the photon polarization angle is fixed θ = 45° and θ = 135°, respectively. (b and d) The calculated spin dependent photoresponse for nanoribbons with one Br atom (1′) removed when the light polarization angle is fixed θ = 45° and θ = 135°, respectively. The width of SbBr nanoribbons is fixed at W = 8. The red, black and blue lines represent the photoresponse for spin up, spin down and charge components.

effect on PGE further. As shown in Fig. 6, we find that the photoresponses with different spin components are equal in magnitude and opposite in direction in the studied photon energy region. The pure spin current is obtained, similar to the BiBr nanoribbon case. By removing a Br atom in position 1′ in the nanoribbon, the magnitude of photoresponse for both spin up and down components is significantly increased. Note that the spin polarization is reduced drastically here. This is mainly because of the backscattering by the defect-induced magnetic edge impurity in the SbBr system, as discussed above. More interestingly, as the photocurrent changes its sign when the photon energy is between 0.05 eV and 0.1 eV in Fig. 6(b and d), the fully spin-polarized photocurrent can also be obtained by introducing a defect into the system. In addition, we also investigated the transport direction of BiBr nanoribbons along the armchair direction, as shown in Fig. 7(a). First, we calculated the band structure of the nanoribbon in Fig. 7(b). It can be found that the edge states also exist along the armchair direction. Next, we investigated the photoresponse generated by PGE in the pristine nanoribbon irradiated by linearly polarized light with different incident photon energies. As shown in Fig. 7(c) and (d), since there is no mirror symmetry along the armchair direction, the generated charge current is non-zero, and the spin-polarized current is generated. When a Br defect is introduced, as shown in Fig. 7(a), the photoresponse will also significantly increase. Still, the photoresponse is no longer close to the pure spin current due to the lack of mirror symmetry. Therefore, like the zigzag direction, the photoresponse along the armchair

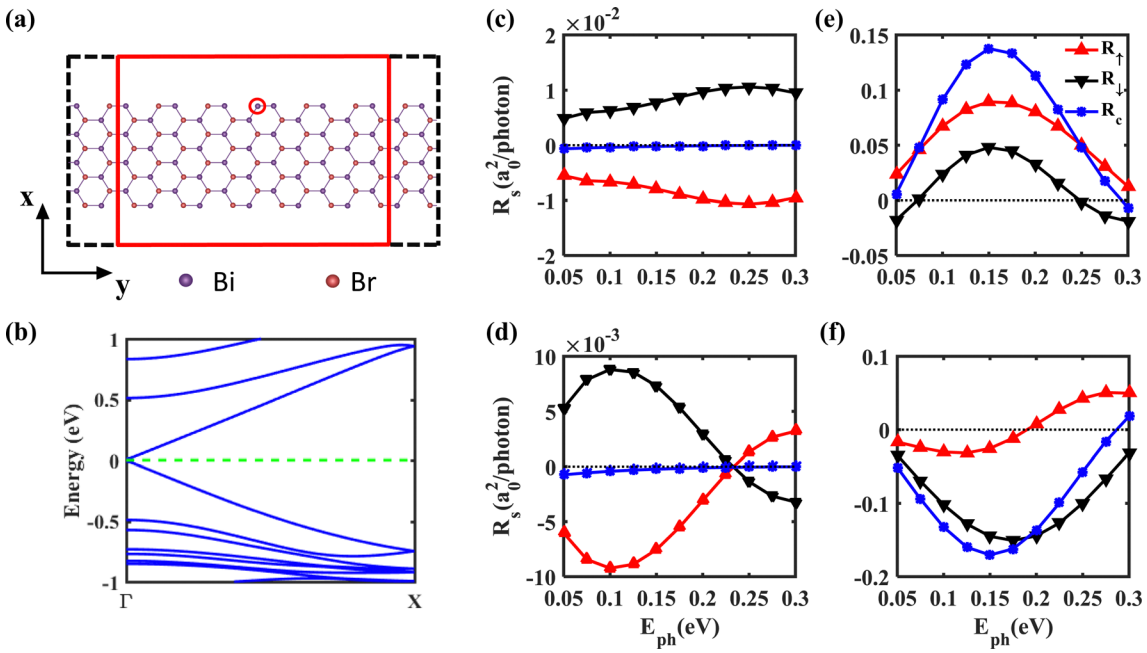

Fig. 7 (a) Top view of the atomic structure of a two-probe device constructed by BiBr armchair nanoribbon with width W = 8. The red circle indicates the position of the vacancy defect where the Br atom is removed. (b) The band structure of BiBr armchair direction nanoribbon. (c–f) The spin-dependent photoresponse R_s *versus* the photon energy E_{ph} of the vertically incident linearly polarized light. (c and d) The calculated spin-dependent photoresponse for pristine BiBr armchair direction nanoribbons when the photon polarization angle is fixed θ = 45° and θ = 135°, respectively. (e and f) The calculated spin-dependent photoresponse for nanoribbons with one Br atom removed when the photon polarization angle is fixed θ = 45° and θ = 135°, respectively.

direction is also sensitive to defects. Thus, the PGE induced photoresponse *via* QSHES depends on the defect.

4 Conclusions

To summarize, we study the photogalvanic effect (PGE) induced spin dependent photoresponse in topological insulators BiBr and SbBr nanoribbons from atomic first-principles calculations. In the pristine system, the pure spin current can be easily obtained. It is found that, although the dc transport properties of QSHES are robust against defects, the photocurrent generated by these edge states *via* PGE is sensitive to defects. The vacancy defect positions can severely affect the generated spin-dependent photoresponse. More importantly, when introducing defects, by tuning the incident photon energies, polarization, and incident angles, the spin related photocurrent can be largely tuned, which paves the way for the novel application of topological insulator nanoribbons in opto-spintronics.

Conflicts of interest

There are no conflicts to declare.

Acknowledgements

We gratefully acknowledge the support from the National Key R&D Program of China under Grant No. 2022YFA1404003, the National Natural Science Foundation of China (Grants No. 12074230, 11974355, and 12174231), the Fund for Shanxi "1331 Project", Shanxi Province 100-Plan Talent Program, Fundamental Research Program of Shanxi Province through 202103021222001. This research was partially conducted using the High Performance Computer of Shanxi University.

References

1 L. Fu and C. L. Kane, *Phys. Rev. B: Condens. Matter Mater. Phys.*, 2007, **76**, 045302.
2 J. E. Moore, *Nature*, 2010, **464**, 194–198.
3 S. Ryu, A. P. Schnyder, A. Furusaki and A. W. Ludwig, *New J. Phys.*, 2010, **12**, 065010.
4 M. Z. Hasan and C. L. Kane, *Rev. Mod. Phys.*, 2010, **82**, 3045.
5 X. Qi and S. Zhang, *Rev. Mod. Phys.*, 2011, **83**, 1057.
6 F. Schindler, A. M. Cook, M. G. Vergniory, Z. Wang, S. S. Parkin, B. A. Bernevig and T. Neupert, *Sci. Adv.*, 2018, **4**, eaat0346.
7 Y. Tokura, K. Yasuda and A. Tsukazaki, *Nat. Rev. Phys.*, 2019, **1**, 126–143.
8 B. I. Halperin, *Phys. Rev. B: Condens. Matter Mater. Phys.*, 1982, **25**, 2185.
9 C. L. Kane and E. J. Mele, *Phys. Rev. Lett.*, 2005, **95**, 226801.
10 R. Chu, J. Shi and S. Shen, *Phys. Rev. B: Condens. Matter Mater. Phys.*, 2011, **84**, 085312.
11 M. Wada, S. Murakami, F. Freimuth and G. Bihlmayer, *Phys. Rev. B: Condens. Matter Mater. Phys.*, 2011, **83**, 121310.
12 L. Zhang, J. Zhuang, Y. Xing, J. Li, J. Wang and H. Guo, *Phys. Rev. B: Condens. Matter Mater. Phys.*, 2014, **89**, 245107.
13 A. Farrell and T. Pereg-Barnea, *Phys. Rev. B*, 2016, **93**, 045121.
14 Y. Nakajima, P. Syers, X. Wang, R. Wang and J. Paglione, *Nat. Phys.*, 2016, **12**, 213–217.
15 K. Hashimoto, X. Wu and T. Kimura, *Phys. Rev. B*, 2017, **95**, 165443.
16 Y. Li, J. Zhang, Y. Wang, H. Du, J. Wu, W. Liu, F. Mei, J. Ma, L. Xiao and S. Jia, *Light: Sci. Appl.*, 2022, **11**, 13.
17 C. Wu, B. A. Bernevig and S.-C. Zhang, *Phys. Rev. Lett.*, 2006, **96**, 106401.
18 D. Pesin and A. H. MacDonald, *Nat. Mater.*, 2012, **11**, 409–416.
19 L. He, X. Kou and K. L. Wang, *Phys. Status Solidi RRL*, 2013, **7**, 50–63.
20 W. Tian, W. Yu, J. Shi and Y. Wang, *Materials*, 2017, **10**, 814.
21 L. Šmejkal, Y. Mokrousov, B. Yan and A. H. MacDonald, *Nat. Phys.*, 2018, **14**, 242–251.
22 C.-H. Hsu, Z.-Q. Huang, F.-C. Chuang, C.-C. Kuo, Y.-T. Liu, H. Lin and A. Bansil, *New J. Phys.*, 2015, **17**, 025005.
23 F. Reis, G. Li, L. Dudy, M. Bauernfeind, S. Glass, W. Hanke, R. Thomale, J. Schäfer and R. Claessen, *Science*, 2017, **357**, 287–290.
24 G. Li, W. Hanke, E. M. Hankiewicz, F. Reis, J. Schäfer, R. Claessen, C. Wu and R. Thomale, *Phys. Rev. B*, 2018, **98**, 165146.
25 M. Hohenadler and F. F. Assaad, *J. Phys.: Condens. Matter*, 2013, **25**, 143201.
26 C. Si, J. Liu, Y. Xu, J. Wu, B.-L. Gu and W. Duan, *Phys. Rev. B: Condens. Matter Mater. Phys.*, 2014, **89**, 115429.
27 L. Kou, Y. Ma, Z. Sun, T. Heine and C. Chen, *J. Phys. Chem. Lett.*, 2017, **8**, 1905–1919.
28 Y. Ren, Z. Qiao and Q. Niu, *Phys. Rev. Lett.*, 2020, **124**, 166804.
29 M. Knig, S. Wiedmann, C. BrÍźne, A. Roth and S. C. Zhang, *Science*, 2007, **318**, 766–770.
30 I. Knez, R. R. Du and G. Sullivan, *Phys. Rev. Lett.*, 2011, **107**, 136603.
31 Y. Tanaka, Z. Ren, T. Sato, K. Nakayama, S. Souma, T. Takahashi, K. Segawa and Y. Ando, *Nat. Phys.*, 2012, **8**, 800–803.
32 C. Chang, J. Zhang, X. Feng, J. Shen, Z. Zhang, M. Guo, K. Li, Y. Ou, P. Wei and L. Wang, *et al.*, *Science*, 2013, **340**, 167–170.
33 Z. Song, C.-C. Liu, J. Yang, J. Han, M. Ye, B. Fu, Y. Yang, Q. Niu, J. Lu and Y. Yao, *NPG Asia Mater.*, 2014, **6**, e147–e147.
34 L. Vannucci, T. Olsen and K. S. Thygesen, *Phys. Rev. B*, 2020, **101**, 155404.
35 P. Hosur, *Phys. Rev. B: Condens. Matter Mater. Phys.*, 2011, **83**, 035309.
36 S. N. Artemenko and V. Kaladzhyan, *JETP Lett.*, 2013, **97**, 82–86.
37 P. Olbrich, L. Golub, T. Herrmann, S. Danilov, H. Plank, V. BelŕKov, G. Mussler, C. Weyrich, C. Schneider and J. Kampmeier, *et al.*, *Phys. Rev. Lett.*, 2014, **113**, 096601.

38 K. N. Okada, N. Ogawa, R. Yoshimi, A. Tsukazaki, K. S. Takahashi, M. Kawasaki and Y. Tokura, *Phys. Rev. B*, 2016, **93**, 081403.
39 J. Yu, L. Xia, K. Zhu, Q. Pan, X. Zeng, Y. Chen, Y. Liu, C. Yin, S. Cheng and Y. Lai, *et al.*, *ACS Appl. Mater. Interfaces*, 2020, **12**, 18091–18100.
40 G. Kresse and J. Furthmüller, *Phys. Rev. B: Condens. Matter Mater. Phys.*, 1996, **54**, 11169–11186.
41 J. Taylor, H. Guo and J. Wang, *Phys. Rev. B: Condens. Matter Mater. Phys.*, 2001, **63**, 245407.
42 M. Zhai, X. Wang, P. Vasilopoulos, Y. Liu, Y. Dong, L. Zhou, Y. Jiang and W. You, *Nanoscale*, 2014, **6**, 11121–11129.
43 A. Saraiva-Souza, M. Smeu, L. Zhang, M. A. Ratner and H. Guo, *J. Phys. Chem. C*, 2016, **120**, 4605–4611.
44 L. Zhang, Z. Yu, L. Zhang, X. Zheng, L. Xiao, S. Jia and J. Wang, *J. Mater. Chem. C*, 2018, **6**, 2460–2466.
45 For details of the NanoDcal quantum tranpsort package, see, **http://www.hzwtech.com**.
46 L. Zhang, K. Gong, J. Chen, L. Liu, Y. Zhu, D. Xiao and H. Guo, *Phys. Rev. B: Condens. Matter Mater. Phys.*, 2014, **90**, 195428.
47 D. Waldron, P. Haney, B. Larade, A. MacDonald and H. Guo, *Phys. Rev. Lett.*, 2006, **96**, 166804.
48 L. Kleinman and D. Bylander, *Phys. Rev. Lett.*, 1982, **48**, 1425.
49 J. P. Perdew, K. Burke and M. Ernzerhof, *Phys. Rev. Lett.*, 1996, **77**, 3865.
50 L. E. Henrickson, *J. Appl. Phys.*, 2002, **91**, 6273–6281.
51 J. Chen, Y. Hu and H. Guo, *Phys. Rev. B: Condens. Matter Mater. Phys.*, 2012, **85**, 155441.
52 L. V. Keldysh, *Soviet Physics - JETP*, 1965, **20**, 1018–1026.
53 M. Bonitz, R. Nareyka and D. Semkat, *Progress in non-equilibrium Green's functions*, World Scientific Publishing, Singapore, 2000.
54 P. I. Arseev, *Phys.-Usp.*, 2015, **58**, 1159.
55 H. Haug and A.-P. Jauho, *Quantum kinetics in transport and optics of semiconductors*, Springer, 2008, vol. 2.
56 E. Ivchenko and G. Pikus, *JETP Lett.*, 1978, **27**, 604–608.
57 Y. Xie, L. Zhang, Y. Zhu, L. Liu and H. Guo, *Nanotechnology*, 2015, **26**, 455202.
58 S. Ganichev, E. Ivchenko, V. Bel'kov, S. Tarasenko, M. Sollinger, D. Weiss, W. Wegscheider and W. Prettl, *Nature*, 2002, **417**, 153–156.
59 C. Jiang, V. Shalygin, V. Y. Panevin, S. N. Danilov, M. Glazov, R. Yakimova, S. Lara-Avila, S. Kubatkin and S. Ganichev, *Phys. Rev. B: Condens. Matter Mater. Phys.*, 2011, **84**, 125429.
60 Y. Xie, M. Chen, Z. Wu, Y. Hu, Y. Wang, J. Wang and H. Guo, *Phys. Rev. Appl.*, 2018, **10**, 034005.
61 H. Xu, H. Wang, J. Zhou and J. Li, *Nat. Commun.*, 2021, **12**, 1–9.
62 J. Chen, L. Zhang, L. Zhang, X. Zheng, L. Xiao, S. Jia and J. Wang, *Phys. Chem. Chem. Phys.*, 2018, **20**, 26744–26751.
63 X. Tao, P. Jiang, H. Hao, X. Zheng, L. Zhang and Z. Zeng, *Phys. Rev. B*, 2020, **102**, 081402.
64 R. Xiao, D.-F. Shao, Y. Li and H. Jiang, *npj Quantum Mater.*, 2021, **6**, 1–6.
65 L. Zhang, J. Chen, L. Zhang, F. Xu, L. Xiao and S. Jia, *Carbon*, 2021, **173**, 565–571.
66 H. Xu, H. Wang, J. Zhou and J. Li, *Nat. Commun.*, 2021, **12**, 1–9.
67 J. Zhao, Y. Hu, Y. Xie, L. Zhang and Y. Wang, *Phys. Rev. Appl.*, 2020, **14**, 064003.

